A census of the Carina Nebula – II. Energy budget and global properties of the nebulosity

Nathan Smith[1]★ and Kate J. Brooks[2]★

[1]*Astronomy Department, University of California, 601 Campbell Hall, Berkeley, CA 94720, USA*
[2]*Australia Telescope National Facility, CSIRO, PO Box 76, Epping, NSW 1710, Australia*

ABSTRACT

The first paper in this series took a direct census of energy input from the known OB stars in the Carina Nebula, and in this paper we study the global properties of the surrounding nebulosity. This detailed comparison may prove useful for interpreting observations of extragalactic giant H II regions and ultraluminous infrared (IR) galaxies. We find that the total IR luminosity of Carina is about $1.2 \times 10^7 \, L_\odot$, accounting for only about 50–60 per cent of the known stellar luminosity from Paper I. Similarly, the ionizing photon luminosity derived from the integrated radio continuum is about $7 \times 10^{50} \, s^{-1}$, accounting for $\sim$75 per cent of the expected Lyman continuum from known OB stars. The total kinetic energy of the nebula is about 8×10^{51} erg, or $\sim$30 per cent of the mechanical energy from stellar winds over the lifetime of the nebula, so there is no need to invoke a supernova (SN) explosion based on energetics. Warm dust grains residing in the H II region interior dominate emission at 10–30 μm, but cooler grains at 30–40 K dominate the IR luminosity and indicate a likely gas mass of $\sim 10^6 \, M_\odot$. We find an excellent correlation between the radio continuum and 20–25 μm emission, consistent with the idea that the $\sim$80-K grain population is heated by trapped Lyα photons. Similarly, we find a near perfect correlation between the far-IR optical depth map of cool grains and 8.6-μm hydrocarbon emission, indicating that most of the nebular mass resides as atomic gas in photodissociation regions and not in dense molecular clouds. Synchronized star formation around the periphery of Carina provides a strong case that star formation here was indeed triggered by stellar winds and ultraviolet radiation. This second generation appears to involve a cascade toward preferentially intermediate- and low-mass stars, but this may soon change when η Carinae and its siblings explode. If the current reservoir of atomic and molecular gas can be tapped at that time, massive star formation may be rejuvenated around the periphery of Carina much as if it were a young version of Gould's Belt. Furthermore, when these multiple SNe occur, the triggered second generation will be pelted repeatedly with SN ejecta bearing short-lived radioactive nuclides. Carina may therefore represent the most observable analogue to the cradle of our own Solar system.

Key words: stars: formation – H II regions – ISM: individual: NGC 3372.

1 INTRODUCTION

The Carina Nebula (NGC 3372) is the nearest massive star-forming region that satisfies three criteria which distinguish it from other Galactic giant H II regions: (1) it harbours the most extreme grouping of massive stars within a few kpc of the Sun, including $\sim$70 O stars initially (some, like η Carinae (η Car), have now moved off the main sequence) that are in the process of creating a giant

superbubble; (2) it is young enough that active star formation is still ongoing within a few parsecs of these massive stars and (3) unlike any comparable massive cluster in our Galaxy, our sightline to it suffers little interstellar extinction, allowing it to be studied across the electromagnetic spectrum and not just at infrared (IR) and radio wavelengths. This last point is critical, because it offers the potential to construct a relatively complete picture of the massive star-forming environment and the stellar content. The first two indicate that Carina is our nearest suitable analogue of more extreme regions like 30 Doradus (30 Dor). Finally, unlike many Galactic regions, the distance to Carina (2.3 kpc) is known to within a few per cent from

★E-mail: nathans@astro.berkeley.edu (NS); Kate.Brooks@csiro.au (KJB)

the expansion parallax of η Car's circumstellar nebula (see Allen & Hillier 1993; Smith 2002b, 2006b), so that the properties one derives are reliable.

In this paper we aim to assess the total energy budget of the region and the global properties of the large-scale nebulosity. In a previous paper (Smith 2006a, hereafter Paper I) we compiled the total energy input from the known stellar population, including both radiation and mechanical energy from stellar winds. Thus, with the energy input known, we can evaluate the efficiency with which stellar radiation is reprocessed by the gas and dust. Carina is an ideal laboratory for comprehensive multiwavelength studies of an environment much like that where our own Solar system may have formed, where young protoplanetary discs will be bombarded by supernova (SN) ejecta. It also represents the early stages of the birth of an OB association, and it is an environment where this young OB association is triggering the birth of a second generation of stars as they destroy their own natal giant molecular cloud.

Our goals here are twofold. First, we wish to evaluate the global energy budget of the entire Carina Nebula by examining its overall, average observed properties, much as if it were an unresolved extragalactic giant H II region. We can then compare this nebular energy budget with the known stellar energy input (Paper I). This provides a check on the validity of deriving stellar properties using similar observations of more distant H II regions where the stars cannot be counted individually (e.g. Kennicutt 1984, 1998), as well as the most extreme examples of star formation in ultraluminous infrared galaxies (ULIRGs). Second, we examine large-scale correlations between various tracers of ionized gas, polycyclic aromatic hydrocarbons (PAHs) and warm and cold dust properties, providing more complete insight to the global structure of giant H II regions.

2 MULTIWAVELENGTH OBSERVATIONS

2.1 Visual-wavelength images

We incorporate wide-field optical images of the Carina region taken through narrow-band filters transmitting [O III] λ5007, Hα and [S II] $\lambda\lambda$6717, 6731, as well as images through the broad-band *B* and *R* filters. The images were already presented and discussed briefly by Smith et al. (2000), and were obtained in 1999 April as part of the Mount Stromlo and Siding Spring Observatory (MSSSO) Hα survey (Buxton, Bessell & Watsson 1998). See Smith et al. (2000) for more details. Fig. 1(a) shows a three-colour version of the [O III] + Hα + [S II] image. The Hα filter is contaminated by emission from [N II] λ6583, but this effect is less than 5 per cent over the brightest parts of the nebula (Smith, Barbá & Walborn 2004b). While the [N II]/Hα ratio rises in ionization fronts at the edges of the nebula, these faint outer regions contribute little to the total Hα flux. The narrow-band images used here were flux calibrated in erg s^{-1} cm^{-2} arcsec^{-2} (integrated over each filter bandwidth) by matching counts in diffuse regions near the Keyhole nebula to the observed surface brightness in the same regions in flux-calibrated images of the Keyhole obtained with *Hubble Space Telescope*/Wide-Field Planetary Camera 2 (*HST*/WFPC2; see Smith et al. 2004b). The calibrated images have been corrected for an average interstellar extinction of $E(B - V) = 0.4$ and $R = 4.8$ indicated by nebular gas in that part of the inner Carina Nebula (Smith 2002a; Smith et al. 2004b), but obviously this does not correct for patches of local extinction by dark clouds.

2.2 Mid-IR: *MSX*

The Carina Nebula was observed by the *Midcourse Space Experiment* (*MSX*) satellite, which is a Ballistic Missile Defense Organization satellite launched in 1996 April, equipped with a 33-cm diameter telescope and IR imager called SPIRIT III. Details of the instrumentation are given by Egan et al. (1998), while a description of the astronomical experiments is given by Price (1995). A brief initial discussion of the *MSX* observations of Carina was already given by Smith et al. (2000), but a more thorough analysis will be undertaken here. We consider observations of Carina obtained in four filters: band A ($\Delta\lambda = 6.8$–10.8 μm), band C ($\Delta\lambda = 11$–15.3 μm), band D ($\Delta\lambda = 13$–16.5 μm) and band E ($\Delta\lambda = 17.5$–27.5 μm). In general, for extended regions, band A is dominated by PAH emission features, while band E is dominated by thermal continuum emission from hot dust grains. Band E also includes a broad 21.3 μm emission feature, presumably caused by silicate emission, which is strong in the inner Carina Nebula (Chan & Onaka 2000) and the supernova remnant (SNR) Cas A (Arendt, Dwek & Moseley 1999). The effective spatial resolution in these images is about 18 arcsec or better.

Several individual image tiles for each filter were obtained from the archive at the Infrared Processing and Analysis Center (IPAC) and mosaiced together to produce a wide-field image of the entire region. The resulting mosaic images in each filter were then spatially aligned with the optical images, resulting in a pixel scale of 12.35 arcsec and a total field of view of $2.8 \times 4 \deg^2$, as shown in Fig. 1(b). The original image data were calibrated in irradiance units of W m^{-2} sr^{-1}. In order to measure the total flux from the region, we converted these to Jy arcsec^{-2} using the bandwidth of each filter.

2.3 Far-IR: *IRAS*

As with the *MSX* data, we used the IPAC archive to retrieve several tiled images obtained by the *Infrared Astronomical Satellite* (*IRAS*). We mosaiced together the individual tiles into a large image in each of the four *IRAS* bands (12, 25, 60 and 100 μm), and then spatially aligned these to the optical and *MSX* images. The result is shown in Fig. 1(c). We did not use higher resolution *IRAS* images at 60 and 100 μm from the *IRAS* Galaxy Atlas because we are most interested in global properties, and we need accurate absolute fluxes to investigate dust colour temperatures and optical depths from image ratios at various wavelengths.

2.4 Radio data

In order to measure the total radio continuum flux as a proxy for the ionizing flux in the nebula, we need a radio continuum map that covers the whole Carina region with single-dish data. This is because flux at low spatial frequencies is lost in interferometric data like that from the Molonglo Observatory Synthesis Telescope (MOST) presented by Whiteoak (1994), although we will use those data for investigating the multiwavelength morphology.

To date, the best single-dish radio continuum map of Carina is still the 3.4-cm continuum map made over 30 yr ago by Huchtmeier & Day (1975). This map, obtained with the 64-m Parkes telescope, has an effective spatial resolution of $\sim$2.6 arcmin, comparable to the *IRAS* data. Unfortunately, the data were not available to us in digital form. Therefore, we used a crude technique to digitize the contour map published by Huchtmeier & Day (1975) into a FITS (Flexible Image Transport System) file (i.e. we drew a grid over the original contour map, and read-off the intensity in each pixel, interpolating when necessary). This yielded a map of the 3.4-cm
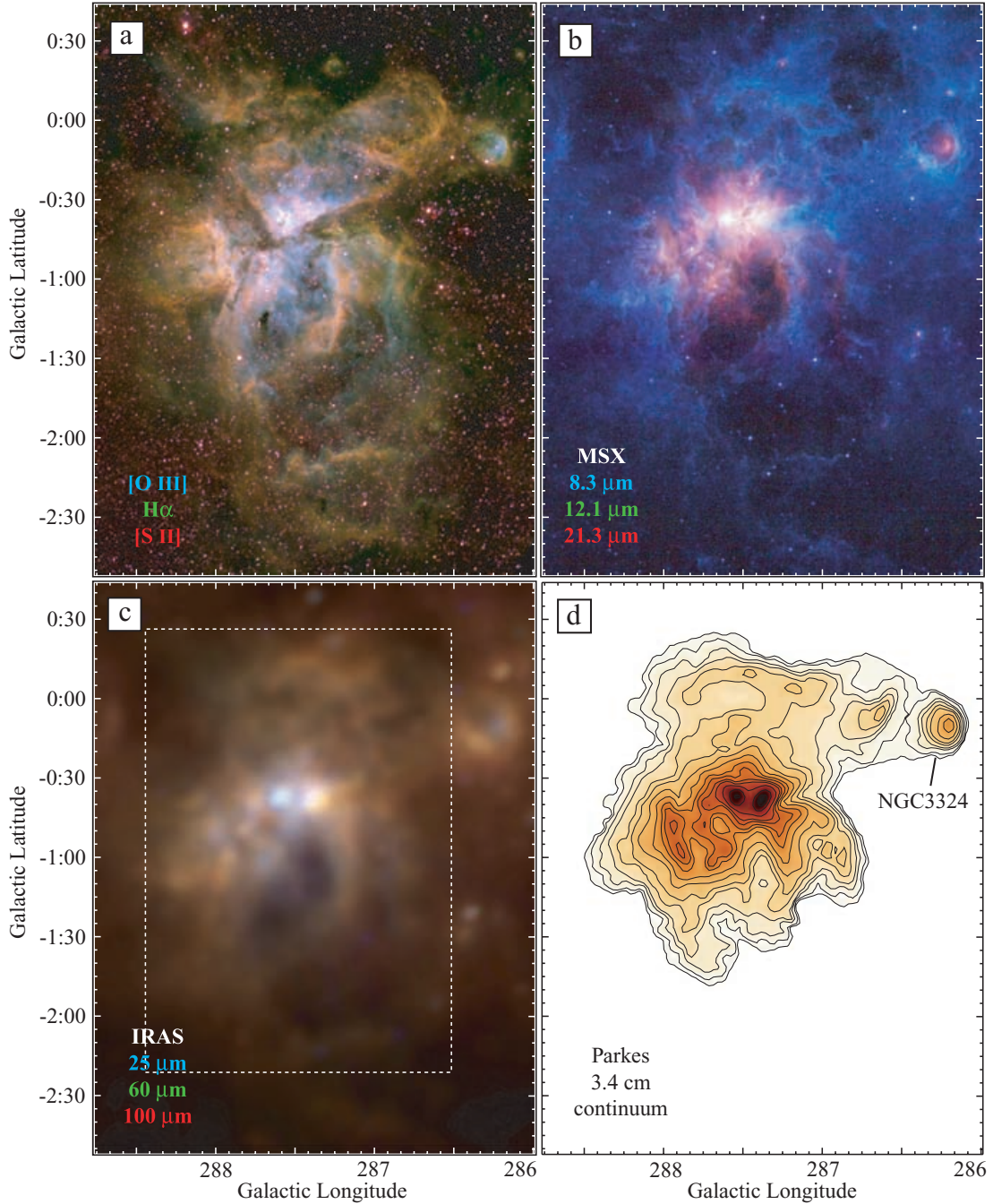
Figure 1. Wide field images of the entire Carina Nebula in the optical, IR and radio. (a) Composite colour image with blue = [O III] λ5007, green = Hα and red = [S II] λλ6717, 6731 (from Smith et al. 2000). (b) Colour image from *MSX* data, with blue = band A, green = band C and red = band E. (c) Colour image from *IRAS* data, with blue = 25 μm, green = 60 μm and red = 100 μm. (d) False colour image of the 3.4-cm radio continuum measured by the Parkes telescope (see Huchtmeier & Day 1975). The dashed rectangle in panel (c) is the region over which we integrated the total fluxes for the nebula at all wavelengths. Galactic coordinates are measured in degrees. η Car and the centre of Tr 16 are located at $l, b = 287°36', -0°38'$, while Tr 14 is at $l, b = 287°25', -0°36'$.

intensity over most of the nebula, shown in Fig. 1(d), which can then be used to measure the integrated 3.4-cm flux and the spatial distribution of free–free radio emission. This map is missing some low surface brightness emission in the outer nebula, which can be seen in the Hα image but is below the lowest radio contour level. This low-level emission should contribute less than ~10 per cent of the total flux, which is less than the uncertainty.

Additional radio data will be considered later in this paper as well. To examine the spatial distribution of 0.843 GHz radio contin-

uum emission at higher spatial resolution (roughly 30 arcsec), we will examine the MOST maps from Whiteoak (1994), as mentioned above. These data were obtained from the online Molonglo Galactic Plane Survey (MGPS) made with the MOST telescope.[1] To compare the distribution of molecular gas in giant molecular clouds, we will use the emission maps of Carina obtained by the recent ^{12}CO(1–0)

---

[1] www.physics.usyd.edu.au/astrop/most

Table 1. Total measured fluxes.

λ (μm)	ID	Units	Flux	Error
0.501	[O III]	erg s^{-1} cm^{-2}	2.12($-$7)	5 per cent
0.656	Hα	erg s^{-1} cm^{-2}	6.40($-$7)	5 per cent
8.3	*MSX* A	Jy	1.54(4)	10 per cent
12.1	*MSX* C	Jy	4.26(4)	10 per cent
14.7	*MSX* D	Jy	3.49(4)	10 per cent
21.3	*MSX* E	Jy	9.55(4)	10 per cent
12	*IRAS* 1	Jy	4.26(4)	10 per cent
25	*IRAS* 2	Jy	1.53(5)	10 per cent
60	*IRAS* 3	Jy	8.75(5)	10 per cent
100	*IRAS* 4	Jy	1.43(6)	10 per cent
34 000	Parkes	Jy	1.43(3)	20 per cent

NANTEN survey of Yonekura et al. (2005), which have an effective beam size of 2.7 arcmin.

3 INTEGRATED NEBULAR PROPERTIES

To evaluate the global mass and energy budget of Carina, we wish to measure the total IR luminosity, the total free–free radio continuum emission and the total Hα flux emitted by the entire nebula. We begin with thermal dust emission.

3.1 The SED and the total IR luminosity

We regard the presence of the exceedingly bright object η Car as anomalous compared to most giant H II regions, since η Car is in a very brief eruptive evolutionary phase. Therefore, we subtracted its direct influence from the total integrated fluxes. Since nearly all of its stellar radiation is reprocessed by circumstellar dust and escapes in the IR (Smith et al. 2003b), radiation from η Car no longer contributes to the radiative energy budget of the H II region. This is appropriate, since in many of the images η Car itself is saturated, and thus, the global integrated flux including η Car would be incorrect anyway. Before summing the total observed flux for each filter within the box in Fig. 1(c), we used IMEDIT in IRAF (Image Reduction and Analysis Facility) to carefully interpolate over η Car, removing its flux from each image. This process was admittedly subjective because of possible confusion between η Car and the diffuse source Car II (the Keyhole Nebula) at some wavelengths. However, the integrated IR to radio spectral energy distribution (SED) of η Car is known well (e.g. Cox et al. 1995; Morris et al. 1999; Smith et al. 2003b; Brooks et al. 2005), providing an independent check on our results, and the complex structure of the Keyhole region including η Car has been observed at higher resolution at optical to radio wavelengths (Whiteoak 1994; Cox & Bronfman 1995; Brooks, Whiteoak & Storey 1998; Brooks et al. 2000; Brooks, Storey & Whiteoak 2001; Smith 2002a; Brooks et al. 2005), which helps minimize confusion. This subtraction is important in Hα and in the mid-IR at 8–30 μm, where η Car itself contributes nearly half of the total flux from the Carina Nebula. However, at the more critical far-IR and radio wavelengths of interest here, η Car's contribution is minimal anyway, as it provides less than 3 and 0.5 per cent of the total emission at 60 and 100 μm, respectively.

Table 1 lists integrated fluxes at each wavelength for the entire Carina Nebula, summed over the region within the dashed rectangular box in Fig. 1(c). This includes most of the observed filaments associated with Carina, but attempts to exclude the emission from the nearby H II region NGC 3324. The total fluxes have been sky subtracted by sampling a region of blank sky at the bottom of the

images, but subtraction of the irregularly varying diffuse emission from the Galactic plane itself was problematic. This was the main source of uncertainty quoted in the last column of Table 1. By sampling nearby regions in the Galactic plane immediately adjacent to Carina, we found that this diffuse emission may contribute as much as $\sim$5 per cent at the shorter mid-IR wavelengths, and possibly as much as 10 per cent of the total flux at 60 and 100 μm. The fluxes in Table 1 have therefore been reduced by these fractions.[2] The Hα and [O III] images were background subtracted before taking the total flux by fitting a surface polynomial to the background Galactic plane emission. These two images were also continuum subtracted before measuring the total flux using a scaled version of the *R*-band image for Hα and an average of the *R*- and *B*-band images for [O III]. Continuum subtraction was not perfect, but the difference in total line flux before and after continuum subtraction was <3 per cent in both filters.

The observed total fluxes from Carina are plotted in Fig. 2, which shows the IR-to-radio SED of the whole nebula. It is striking how similar the SED of Carina is to that of a typical ULIRG (e.g. Sanders & Mirabel 1996). A fit to this SED is shown by the solid curve, using emission from three optically thin grey body (i.e. emissivity $\propto \lambda^{-1}$) components at $T = 220$, 80 and 35 K, plus a simple component from optically thin thermal bremsstrahlung radio continuum emission. We chose three specific dust temperatures because this is the minimum number that can account for the observed SED's shape, but it is possible that the spectrum at mid-IR wavelengths can be approximated by a range of temperatures. However, decomposing the SED into additional components would not significantly alter the estimate of the total luminosity and dust mass (Table 2). Fluxes in the 8.3, 12–12.1 and 21.3 μm filters are allowed to be somewhat above this fit because they may contain strong emission from PAH and silicate emission features at 8.6, 9.7, 11.3 and 22 μm. These emission features suggest that the 220-K component in Fig. 2 and Table 2 does not truly represent continuum emission from hot grains. Hence, the 220-K component's dust mass in Table 2 is listed in parentheses. In any case, the shorter IR wavelengths are unimportant in the mass budget.

The luminosities for each of these three component fits and the total are listed in Table 2. As long as the dust grains are small ($a < 0.2$ μm), the dust mass required to emit this IR luminosity can be expressed independently of the grain radius and emissivity (see Smith & Gehrz 2005), so that

$$M_{\text{dust}} = [(100\rho)/(3\sigma T^6)] L_{\text{IR}}, \qquad (1)$$

where σ is the Stefan–Boltzmann constant. This relation was used to derive the dust masses for each component in Table 2, assuming a typical grain density of about 3 g cm^{-3}. Given our assumption of optically thin emission, the true dust mass may be higher than that given in Table 2 if additional mass can be hidden in dense cloud cores that are optically thick even at far-IR wavelengths. However, given that the peak value of the 60 μm optical depth is only 0.005 and the average is much lower than that (see Section 4.1 and Fig. 4b), any optically thick clumps must constitute a tiny fraction of the solid angle of the nebula, so that the bulk of the far-IR emission is, in fact, dominated by optically thin emitting dust. Optically thick cores may cause submillimetre or millimetre emission in excess

---

[2] The high precision to which the 12.1 μm *MSX* flux matches the 12 μm *IRAS* flux is fortuitous. However, even general agreement despite the differences in resolution and sensitivity reassures us that our method of measuring the integrated flux is sound.
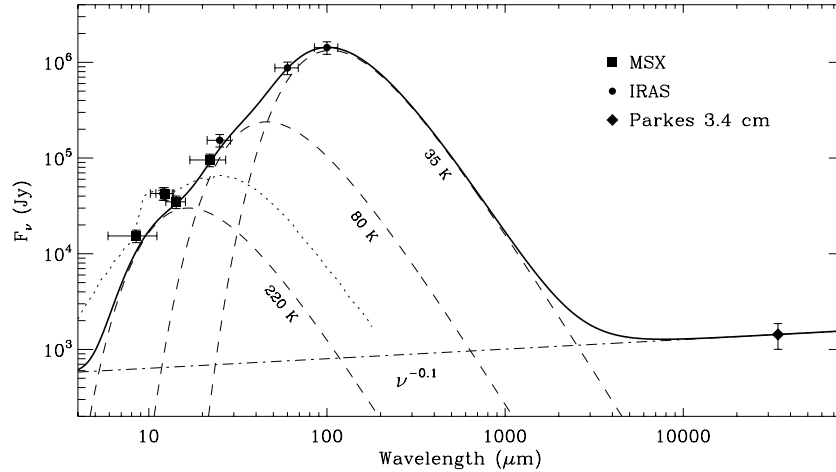
Figure 2. Global IR-to-radio SED of the Carina Nebula. Fluxes were measured within the boundary of the large dashed rectangle in Fig. 1(c), and all have had the flux from η Car subtracted (the IR spectrum of η Car measured by *ISO* is shown by a dotted curve; see Morris et al. 1999; Smith et al. 2003b). Sky and background subtraction were performed as noted in the text.

Table 2. IR dust luminosity and mass.

T (K)	$L/L_\odot$	$M_d/M_\odot$
35	7.6×10^6	9590
80	3.1×10^6	28
220	1.1×10^6	(0.23)
Total	1.18×10^7	9620

of the 35-K component in Fig. 2, and future observations will be useful in that regard. However, preliminary analysis of a 1-mm survey of the brightest parts of the nebula (see Brooks et al. 2005; K. Brooks et al., in preparation), with a 2σ sensitivity equivalent to a $10\,M_\odot$ core at 10 K, suggests an accumulated gas mass in such cold cores of no more than $5000\,M_\odot$. Similarly, Yonekura et al. (2005) detected 15 cores in $C^{18}O$ emission, with a combined mass of only $2.6 \times 10^3\,M_\odot$. Furthermore, the near-perfect correlation between the 60 μm optical depth and the 8.6 μm PAH emission (see Section 4.1) argues that optically thick cores contribute little to the global 60–100 μm emission from Carina.

The total integrated IR luminosity from these three dust components amounts to $\sim 1.2 \times 10^7\,L_\odot$ at a distance of 2.3 kpc. Thus, dust absorbs and reprocesses 50–60 per cent of the available bolometric luminosity from all stars in Carina, which is $\sim 2 \times 10^7\,L_\odot$ (Paper I).[3]

The coolest 35-K component, probably dominated by heating from far-ultraviolet (FUV) photons, contributes about 65 per cent of the IR luminosity or about 40 per cent of the total luminosity. This suggests that about 20 per cent of the FUV radiation escapes through holes in the nebula or is processed by PAH emission, if $L_{FUV}/L_{Bol} \simeq 0.5$ (see Paper I). The 35-K component dominates the emission seen at far-IR wavelengths, in agreement with earlier studies of the far-IR emission from smaller sections of the nebula that inferred dust temperatures of 30–40 K (Harvey, Hoffmann & Campbell 1979; Ghosh et al. 1988).

The warmer 220- and 80-K components that dominate at shorter wavelengths absorb and re-emit the remaining 35 per cent of the IR luminosity, corresponding to only ~ 20 per cent of the total stellar luminosity. As noted earlier, the 220-K population may be erroneous, as would be its associated dust mass estimate, since the shorter mid-IR wavelengths may be dominated by diffuse PAH emission. However, the 80 K-component probably represents warm grains surviving in the interior of the H II region. Throughout most of the nebula, they are heated stochastically by Lyα photons, and therefore, ultimately by Lyman continuum photons (see Section 4.1). Close to the O stars, direct heating of dust by stellar UV continuum radiation may also be important. These 20–25 μm emitting grains are often seen as filamentary structures in the *MSX* band-E image (Fig. 1b); they may reside in dense swept-up shells where the O star winds confront the photoevaporative flows from ionization fronts.

3.2 The mass budget

The cool 35-K component dominates the mass of emitting dust in the nebula. While the warmer components make a substantial contribution to the luminosity, they are irrelevant to the total dust mass. The total mass revealed by thermal dust emission is about $9600\,M_\odot$ (Table 2). The uncertainty in this dust mass is large, perhaps of order ± 20 per cent because of potential errors in background subtraction and uncertain grain properties.[4]

The total mass of molecular gas in the Carina region is estimated to be $6.7 \times 10^5\,M_\odot$ from the Columbia CO survey of the Galactic plane (Grabelsky et al. 1988). The relevant molecular mass is even less than this, since this value was estimated over a region larger than the box in Fig. 1(c). Yonekura et al. (2005) give a smaller value of $3.5 \times 10^5\,M_\odot$. As explained below in Section 4, we favour an interpretation where the mass traced by the far-IR dust emission is probably mixed-in with warm atomic gas in photon-dominated regions (PDRs) behind ionization fronts because it has a different

---

[3] Excluding η Car's luminosity of $5 \times 10^6\,L_\odot$ (Smith et al. 2003b). Most of η Car's radiation escapes in the mid-IR, which has already been subtracted directly from our data.

[4] The mass estimate is dominated by the 35-K component in Fig. 2. This component cannot be hotter or more luminous, but there could be additional mass hidden in cool grains that we are not sensitive to because we do not yet have a global estimate of the submm luminosity of the nebula, as noted earlier.
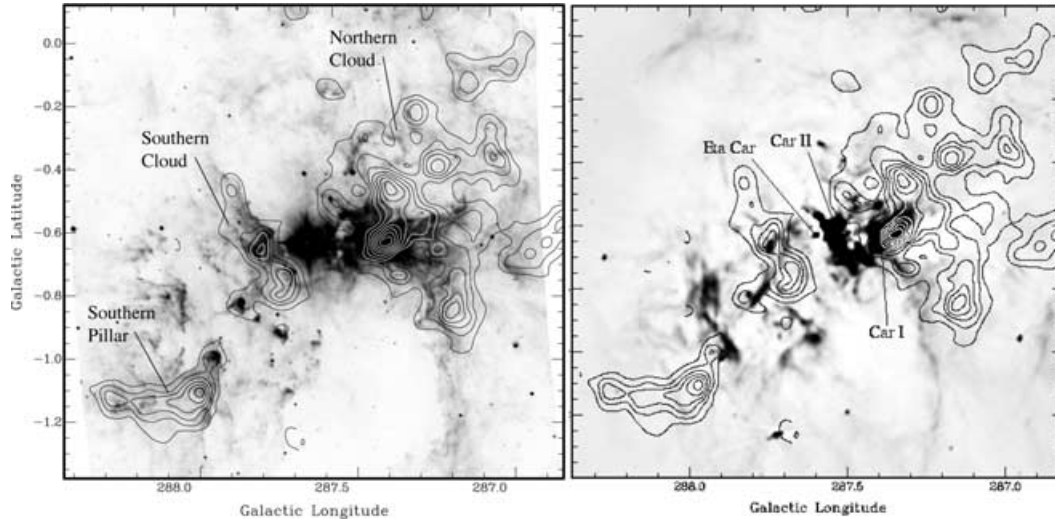
Figure 3. Molecular gas distribution in the Carina Nebula, with contours from the NANTEN ^{12}CO(1–0) survey of Yonekura et al. (2005). These contours are superposed on images at 8 μm from *MSX* (left; Smith et al. 2000) and in the 0.843 GHz continuum from MOST (right; Whiteoak 1994).

spatial distribution than the CO clouds (Fig. 3). Thus, the gas:dust mass ratio inferred from comparing molecular gas and dust is erroneous because the warm emitting dust and the CO gas trace different components of the nebula.

Instead, if we assume that the far-IR emission from ∼35-K dust traces warm atomic gas in PDRs, then a typical gas:dust mass ratio of 100 there would indicate a total gas mass of ∼10^6 M$_\odot$. This, in turn, would indicate that the warm gas in PDRs dominates over molecular clouds in the total mass budget of the nebula. Brooks et al. (2003), however, find that most of the gas-phase carbon is in CO, so a large reservoir of additional mass may be present that is not traced by the warm ∼35-K dust. The gas currently in the molecular phase is less than about one-third of the total mass budget. Thus, adding the molecular and PDR mass together, about 1–2×10^6 M$_\odot$ in the nebula may still be available for further star formation, providing that it can be swept up into dense enough clouds (see Section 4.4).

What is the mass ratio between this gas and the stars in Carina? A complete stellar census is not yet available, but perhaps we can draw preliminary conclusions by scaling from a well-studied region like the Orion Nebula Cluster (ONC). Hillenbrand & Hartmann (1998), for example, find a total number of stars of 2260 and a total stellar mass of 1800 M$_\odot$ for members of the ONC. Now, the number of stars in the ONC with masses above about 10 M$_\odot$ is six and the number of O-type stars is two, while for the first-generation exposed clusters in Carina the corresponding numbers are 127 and 70 (Paper I). This is certainly not a complete census for Carina since there are many early B stars not included in Paper I, and some O stars may still be obscured (e.g. Sanchawala et al. 2007). Scaling from Orion, then, we find likely values for the total number of first-generation stars in Carina of about 5–8×10^4, harbouring a total stellar mass of 4–6×10^4 M$_\odot$. Errors may be as much as a factor of 2 with this crude method, but are likely to be an underestimate if wrong. We undertook a more detailed analysis where we scaled the Trapezium mass function of Muench et al. (2002) so that the slope at high masses agreed with a mass function from the spectral types in Paper I, and then integrated over a range of 0.08–150 M$_\odot$ to get the total mass, but this produced similar results with similar uncertainty. In any case, the total stellar mass in the first-generation stars in Carina is securely above 2×10^4 M$_\odot$, placing it among the

most massive stellar groupings in the Galaxy. This is in agreement with its large Lyman continuum luminosity.

It would appear from this value for the total stellar mass that the global star formation efficiency in Carina has been less than 10 per cent. However, two important considerations suggest that this would likely be a severe underestimate, and that the star formation efficiency of the first-generation clusters could be as high as 30–50 per cent. First, the total gas mass is derived for a very large region, and likely contains mostly pristine gas that did not participate in the formation of the first generation star clusters like Tr 14 and 16. The mass of gas which has been expelled from the inner region of the nebula that was formerly the molecular cloud core is unclear, but it is probably a small fraction of the total nebular mass. Second, the stellar census is surely incomplete, because it ignores the vast number of second-generation stars that are now forming or have recently formed around the periphery of the nebula, which may be comparable to the first generation. An ongoing analysis of *Spitzer* data (Smith et al., in preparation) suggests that the South Pillar region alone contains well over 10^4 new stars. Thus, a census of this younger second generation will be quite interesting.

3.3 The kinetic energy budget, diffuse X-rays and a previous supernova?

If we take the mass of warm atomic gas inferred in the previous section at face value as the dominant mass component, we can evaluate the total kinetic energy budget of the nebula. We found a total gas mass of ∼10^6 M$_\odot$ from the cool dust mass for an assumed normal gas:dust mass ratio of 100.

High-resolution spectroscopic observations of ionized gas in Carina over the past decades have repeatedly established a ubiquitous line splitting of 35–40 km s^{-1} across the entire region (e.g. Deharveng & Maucherat 1975; Walborn & Hesser 1975; Azcarate, Cersosimo & Colomb 1981; Meaburn, Lopez & Keir 1984; Smith, Bally & Brooks 2004a). If we then take ±20 km s^{-1} as representative of the bulk expansion velocity of the developing superbubble cavity (Smith et al. 2000), the implied total kinetic energy of the nebula would be of order 8×10^{51} erg. This agrees well with the value of ∼9×10^{51} erg estimated on different grounds by Smith

et al. (2000); it was the energy needed to sweep up the cavity to the observed size assuming a homogeneous ambient medium.

Although the large kinetic energy budget of the nebula allows for input from one or more past SNe, there is no *need* to invoke a previous SN to account for it. The present kinetic energy of the nebula we derive here is only 30 per cent of the available kinetic energy of 2.6×10^{52} erg supplied by stellar winds throughout the $\sim$3 Myr lifetime of the nebula (Paper I). Thus, the observed kinetic energy budget gives no evidence to alter the view that the Carina Nebula is in an early phase of its expansion still dominated by stellar winds and radiation pressure.[5] This is supported by the lack of any evidence for significant non-thermal radio continuum emission from the nebula. It is also in agreement with Brooks et al. (2003), who find that stellar winds alone can account for the kinematics of the molecular-line data. In that case, the diffuse soft X-ray emission in Carina (Seward et al. 1979; Seward & Chlebowski 1982) could arise from a shock between stellar winds expanding from O stars in Tr 14 and 16 as they collide with the evaporative PDR flow from the surrounding molecular clouds. The intricate structure of the evaporating pillars would make the geometry of this shocked material very irregular, causing strong variations along adjacent lines of sight, while still being present across the whole region. Thus, it is plausible that the high-velocity absorption components (e.g. Walborn & Hesser 1975; Walborn et al. 1984; Danks et al. 2001; Walborn et al. 2007) may result within these wind interaction regions as well.

3.4 Tracers of the ionized gas

The total flux of free–free radio continuum emission is often taken as a diagnostic of the total Lyman continuum luminosity of an H II region, because it avoids potentially large uncertainties in extinction. The total number of hydrogen ionizing photons absorbed by the gas can be expressed as

$$Q_{\mathrm{H}} = 9.09 \times 10^{46}\, T_4^{-0.45} \left(\frac{\nu}{8.82\,\mathrm{GHz}} \right)^{0.1} S_\nu D^2\, \mathrm{s}^{-1}, \tag{2}$$

where T_4 is the assumed electron temperature in units of 10^4 K, S_ν is the observed flux density in Jy at frequency ν and D is the distance in kpc. In equation (2), we have assumed that the $n(\mathrm{He})/n(\mathrm{H})$ abundance is 0.1, that the volume of the He^+ region is half of the H^+ region, and that the fraction of He recombination photons that can ionize H is $f_i = 0.65$ (e.g. Simpson & Rubin 1990). In that case, the factor $(1 + f_i \langle \mathrm{He}^+/[\mathrm{H}^+ + \mathrm{He}^+]\rangle)^{-1}$ is 0.969; it would be 0.939 with equal volumes for the He^+ and H^+ zones, changing our value for Q_{H} by an insignificant 3 per cent.

From Table 1, we measure a total 3.4 cm (8.82 GHz) flux of $S_\nu = 1430$ Jy for the whole nebula, integrated over the large rectangular area in Fig. 1(c). Assuming $T_e = 10^4$ K in equation (2), this flux translates to a total Lyman continuum photon luminosity of $Q_{\mathrm{H}} \simeq 6.9 \times 10^{50}\,\mathrm{s}^{-1}$. This can be compared to our estimate in Paper I of the total Lyman continuum output of the known OB stars in Carina of $Q_{\mathrm{H}} = 9.1 \times 10^{50}\,\mathrm{s}^{-1}$. Thus, it would appear from this analysis that roughly 25 per cent of the ionizing photons may be able

to leak out of Carina.[6] This escape fraction will need to be larger if there remains a significant number of hot stars in Carina that are obscured at visual wavelengths and were not included in the census in Paper I.

Also using radio continuum observations, Brooks et al. (2001) estimated the number of hydrogen ionizing photons absorbed locally by the radio sources Car I and Car II (associated with Tr 14 and 16, respectively). Comparing these values to the expected Lyman continuum output from each cluster in Paper I, it appears that Car I absorbs 5.5 per cent of Tr 14's ionizing radiation, while Car II absorbs much less than 1 per cent of the ionizing photons from Tr 16. This tells us that the vast majority of ionizing radiation from these clusters escapes to large distances in the nebula. It also means that Tr 14 is more involved in dense gas than Tr 16, providing another clue that it may be somewhat younger than Tr 16.

The total Hα luminosity that escapes the nebula (corrected for the average interstellar extinction but not local non-uniform extinction from dark clouds within the nebula) is about 10^5 L$_\odot$, and the escaping luminosity in the [O III] λ5007 line is about 3×10^4 L$_\odot$. This Hα luminosity is about 1/3 that of 30 Dor (Kennicutt 1984).

In studies of extragalactic H II regions and star-forming galaxies, the total Hα luminosity is also used to derive the number of hydrogen ionizing photons. Following Kennicutt (1998),

$$Q_{\mathrm{H}} = 2.93 \times 10^{45} \left(\frac{L_{\mathrm{H}\alpha}}{\mathrm{L}_\odot} \right)\, \mathrm{s}^{-1}, \tag{3}$$

where $L_{\mathrm{H}\alpha}$ is the luminosity in the Hα emission line. For our measured value of $L_{\mathrm{H}\alpha} \simeq 10^5$ L$_\odot$ for the total Hα line luminosity in Carina, we then have $Q_{\mathrm{H}} \simeq 3 \times 10^{50}\,\mathrm{s}^{-1}$. Thus, with standard assumptions the observed Hα flux appears to significantly underestimate the total Lyman continuum flux as measured from the radio continuum (about 40–50 per cent), and it severely (factor of 3) underestimates the expected Lyman continuum luminosity from known O stars (Paper I). Perhaps this is because the Hα line suffers from severe non-uniform extinction. The required average extinction would be an additional $A_R \simeq 0.9$ mag. We corrected the Hα flux for the small amount of average interstellar extinction toward Carina, but not for local extinction; we will see below in Section 4.2 that non-uniform local extinction is severe.

The ratio of the global [O III] λ5007 luminosity to that of Hα for the whole nebula is about 0.3. The observed and dereddened ratio of [O III] λ5007 to Hα in the brightest inner parts of the nebula is $\sim$1 (Smith et al. 2004b). This means that [O III] is more centrally concentrated than Hα, and again, may be more heavily absorbed there due to non-uniform extinction, which is in fact the case as we discuss later in Section 4.2. This suggests caution when interpreting [O III]/Hα ratios in extragalactic H II regions. As noted in Paper I, the large ionizing photon luminosity places Carina among the most extreme star-forming regions in our Galaxy, such as W49 and NGC 3603, although not quite as extreme as the Arches cluster in the Galactic Centre or 30 Dor.

---

[5] There is one interesting caveat here, however. Recent studies of UV spectra of O stars (e.g. Bouret, Lanz & Hillier 2005; Fullerton, Massa & Prinja 2006) suggest that their winds are highly clumped and that their mass-loss rates may be lower than the rates adopted in Paper I, which were from estimates based on moderate clumping factors (Repolust, Puls & Herrero 2004). If the mass-loss rates are indeed reduced much further than assumed in Paper I, then the input mechanical energy from stellar winds may become comparable to the observed expansion energy of the nebula.
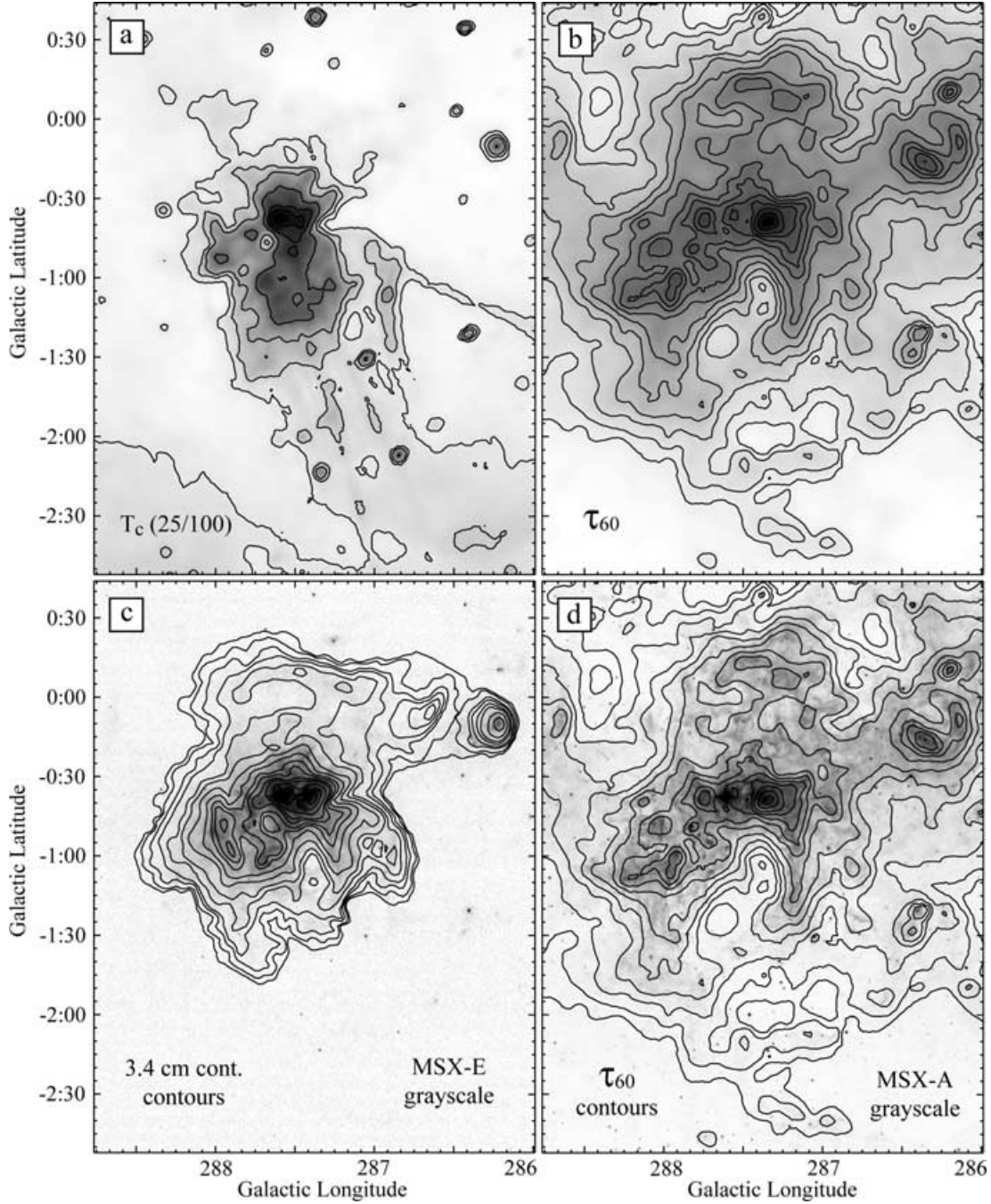
[6] Note, however, that this is the observed value only at the present time, when the dusty Homunculus nebula and η Car's dense wind quench the UV output of η Car and its putative companion (see Paper I). In the recent past (before 1843), the total ionizing flux output of the stars in Carina may have been as high as $Q_{\mathrm{H}} = 11.5 \times 10^{50}\,\mathrm{s}^{-1}$ (Paper I). The ionizing output in this previous state may be relevant even to present observations, since the recombination time-scale in the outer parts of the nebula would be about 50 yr for a typical electron density at ionization fronts of a few $\times 10^3$ cm^{-3} (Smith et al. 2004b), while the light travel time to some outer parts of the nebula is comparable.

Figure 4. (a) Far-IR dust colour temperature made from a ratio of the *IRAS* 25- and 100-μm maps. Contours are drawn at 52, 54, 56, 60, 65 and 70 K. (b) 60 μm emitting optical depth from the *IRAS* 60-μm image and the 25/100 μm dust colour temperature map in panel (a). Optical depth contours are drawn at 3, 4, 6, 9, 13, 20, 30, 50, 70, 100, 140, 200, 320 and 500×10^{-5}. (c) Radio contours from Fig. 1(d) over the *MSX* band-E (21.3 μm) map from Fig. 1(b). (d) 60 μm optical depth contours over the *MSX* band-A (8.3 μm) image.

4 LARGE-SCALE MULTIWAVELENGTH MORPHOLOGY

4.1 Dust distribution

Figs 4(a) and (b) show the far-IR dust colour temperature and 60 μm emitting optical depth, respectively. The temperature map is made from a ratio of the 25 and 100 μm *IRAS* images, while the optical depth map uses this temperature map and the 60-μm *IRAS* image. As noted earlier, we did not use deconvolved images with enhanced resolution, because such images can lead to erroneous features in ratio images, and we are interested primarily in the large-scale distribution (note that we smoothed the 25-μm map to match the spatial resolution of the longer wavelength data). For each pixel, the dust colour temperature and optical depth were calculated in the usual way from ratio images (e.g. Smith et al. 2003b). However, we caution that the numerical values of T and τ in the maps are not necessarily the actual temperature or optical depth of grains in the nebula, since each line of sight may contain multiple grain populations at different temperatures. For example, the SED in Fig. 2 shows that the 25-μm

flux is dominated by warm $\sim$80-K grains across much of the nebula, whereas the 100-µm flux is dominated by cooler $\sim$35-K dust. Therefore, contour levels in Fig. 4 are average values, but are still useful in assessing trends in *relative* dust temperature and column density.

We find an excellent spatial correlation between the large-scale distribution of radio continuum and the 21.3 µm band-E emission from *MSX*, shown in Fig. 4(c). This was noted on smaller scales by Rathborne et al. (2004) and Cox (1995) as well. This is consistent with the interpretation that warm grains in the interior of H II regions are intermixed with and heated *in situ* by emission from the ionized gas itself. For the case B recombination that prevails in most H II regions, Lyα photons trapped in the nebula resonantly scatter many times before being absorbed by dust. Spitzer (1978) showed that for graphite grains bathed in ionized gas with $n_H \simeq 10^3$ cm^{-3} and roughly solar metallicity, the equilibrium temperature from the balance of absorption of trapped Lyα photons and IR emission would be about 80 K. This is, coincidentally, the same temperature we derive for the warm component that dominates the SED at 20–30 µm (Fig. 2). By comparison, a simple estimate indicates that grain–gas collisional energy gain or direct heating by stellar photons is less by at least two orders of magnitude over most of the nebula, although direct UV continuum heating may become important close to the O stars. Some grains in Carina show IR emission features similar to SNRs like Cas A (Chan & Onaka 2000), but there appears to be no need to invoke grain heating by a recent SN to explain the luminosity or temperature of the warm grains.

In general, these results indicate that diffuse 20–30 µm emission that occupies the interiors of similar shell structures can be taken as an excellent tracer of dust that is mixed with dense ionized gas in H II regions. The association of warm grains with ionized gas explains the red emission in the interior of the nebula in the colour *MSX* image in Fig. 1(b), while PAH emission from the surfaces of molecular clouds is seen in blue/green at larger distances from the centre. This pattern clearly holds true in the adjacent region NGC 3324 as well (Fig. 1b), as does the good correlation between 20–25 µm emission and radio continuum (Fig. 4c). This interpretation is probably applicable to H II regions in general. Such features are common in 21.3-µm *MSX* data or in 24-µm images taken by *Spitzer* throughout the Galactic plane (e.g. Churchwell et al. 2006). It would be interesting to see if this type of feature is less obvious at lower metallicity, where the dust:gas ratio is lower.

As interesting, perhaps, is the near-perfect correlation over large scales between the 60 µm optical depth and PAH emission shown in Fig. 4(d), ignoring differences in spatial resolution between *IRAS* and *MSX* images. The only instances where this correlation is not obeyed are for point sources like η Car, embedded protostars and cool giants in the field. However, the 8.6 µm *MSX* band-A emission from these unresolved sources is primarily due to continuum emission from warm circumstellar grains rather than PAH emission. This provides spatially resolved confirmation that the cool 30–40 K dust that dominates the far-IR luminosity measured by *IRAS* – tracing the majority of the nebular mass – resides primarily in warm atomic zones in PDRs heated by the FUV radiation field, and not in colder molecular cloud cores. (The 100 µm optical depth map is essentially the same as the 60 µm optical depth.) The PAH and warm dust distribution is significantly different from that of the molecular cloud cores when examined at the level of detail seen in Fig. 3. On larger size scales where the structure of PDRs is unresolved, the molecular gas and PAH+dust emission do trace one another because the PAH emission comes from the surfaces of molecular clouds. This similar structure on large sizes is due to the clumpy distribution of the gas,

allowing FUV radiation to penetrate to large radii in between the clumps. This view is compatible with the large-scale distribution of high-density molecular gas seen in CO(4–3) and PDR emission seen in [C I] at 610 µm (Zhang et al. 2001).

Earlier we estimated that the difference between IR luminosity and the inferred stellar FUV luminosity in Paper I means that about 20 per cent of this FUV luminosity escapes the nebula. From the large-scale distribution of dust in Fig. 4(b), this may be largely an effect of the asymmetric and clumpy geometry. There is a large hole toward southern Galactic latitudes where a significant fraction of the FUV radiation may escape. It is even apparent in Fig. 4(a) that higher dust temperatures protrude in that direction.

4.2 Extinction distribution and 3D geometry

Fig. 5(a) shows an image of local variations of extinction across the Carina Nebula, derived from a flux ratio image of 3.4 cm radio continuum (Fig. 1d) to a smoothed version of the Hα image. The radio free–free emission and the intrinsic Hα emission should have the same spatial distribution, so dark regions in the grey-scale image correspond to regions of higher visual-wavelength extinction. Thus, we take the radio image as representing an intrinsic surface brightness map of the nebula, I_0, whereas Hα suffers significant extinction from dust at visual wavelengths, causing the apparent surface brightness I to be very different. When we normalize these maps to have the same value in the brighter and less obscured regions of the nebula (where I_0/I has a minimum value, set to 1), regions where ionized gas suffers substantial absorption from foreground clouds have larger values of I_0/I. In all cases, the values of I_0/I shown in Fig. 5(a) may be underestimates, because this map gives the extinction averaged over the 2.6-arcmin beam of the 3.4-cm image, whereas higher resolution optical images show complex small-scale structure. The high values of I_0/I near the top of Fig. 5(a) may be caused by low emission levels near edges of the field.

In the central regions of the nebula, the distribution of local extinction follows the general spatial distribution of the most prominent CO emission as seen in Fig. 3, as well as that of the bright 8 µm PAH emission at molecular cloud surfaces. The main concentrations of molecular gas in the Northern Cloud, the Southern Cloud and the Southern Pillar are all clearly seen as local maxima in the extinction map in Fig. 5(a). The Southern Pillar seems less prominent in the extinction map than in the CO map, suggesting that the bulk of the dust and molecular gas there may be behind much of the ionized gas along the line of sight. Some of the other pillars are known to be on the far side of the nebula as well, based on their line-of-sight extinction patterns or kinematic properties (Smith et al. 2004a, 2005b).

Part of the V-shaped dark dust lane that crosses the centre of the nebula can be seen as a bridge between the Northern and Southern clouds in the extinction map, whereas this bridge is not clearly seen in the CO map. This indicates that the middle parts of this dust lane have fairly low column density compared to other parts of the clouds, with $I_0/I \simeq 2$–3, corresponding to 6563-Å extinction of 0.75–1.2 mag. However, they figure prominently in optical images because they are on the near side of the nebula.

The strongest regions of extinction, corresponding to the Northern and Southern clouds, have peak values for I_0/I of roughly 10 and 20, respectively, corresponding to extinctions at 6563 Å of 2.5 and 3.3 mag. These regions suffering high extinction correspond to areas of strong intrinsic emission. This non-uniform extinction that blocks some of the brightest Hα emission in the centre of the nebula is the qualitative explanation for why Q_H derived from the total
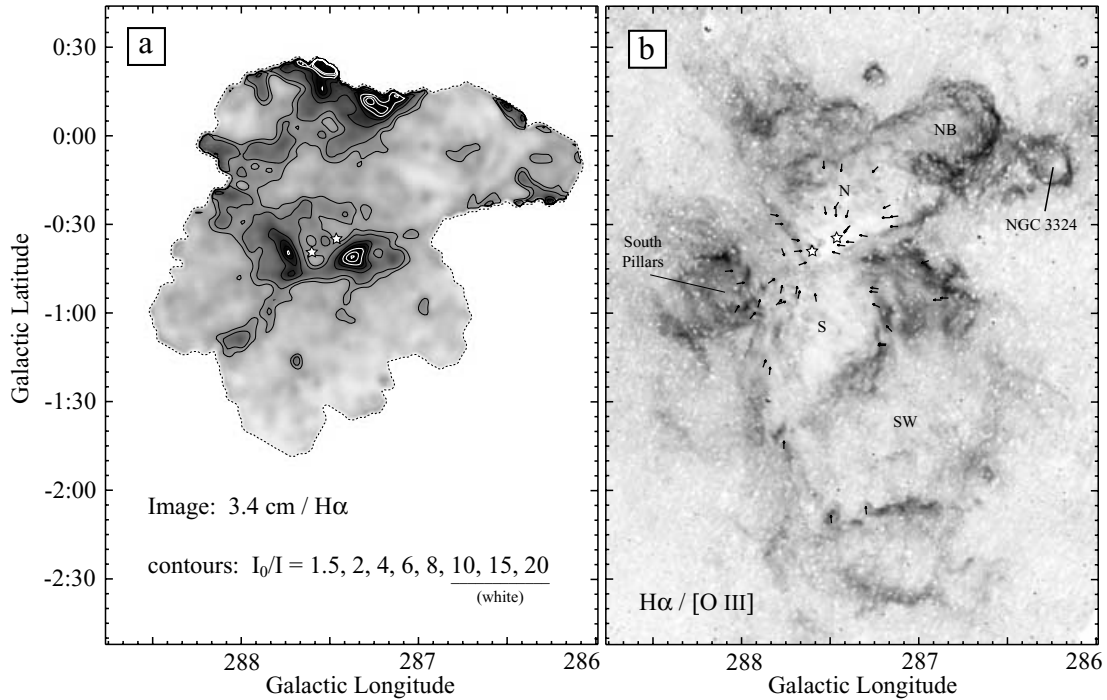
Figure 5. (a) Flux ratio image of 3.4-cm continuum to Hα. The Hα image was blurred to match the spatial resolution of the radio image in Fig. 1(d). Contours of I_0/I are shown, where I_0/I is derived with the radio/Hα ratio normalized to unity across optically bright regions of the nebula (the dashed line is not a contour; it simply marks the boundary of the radio continuum image). I_0/I therefore traces strong local variations in extinction across the nebula, where darker regions (higher values of I_0/I) have stronger line-of-sight extinction. The regions of high extinction at the top edge of the nebula correspond to regions of low surface brightness. (b) Flux ratio image of Hα to [O III] λ5007, which shows shell-like structures that arise at the edges of large cavities. Short arrows mark the orientations of 'directional indicators' like cometary clouds and dust pillars (see text). The two stars in both panels mark the approximate locations of the star clusters Tr 14 and 16; Tr 16 is the one on the left, although the stars in Tr 16 are spread over a larger area than this symbol.

Hα luminosity is smaller than Q_H derived from the radio continuum. Namely, even though we corrected the total Hα luminosity for interstellar extinction to Carina using average values of $E(B-V)$ derived from optical spectra (e.g. Smith et al. 2004b), this method did not correct for the non-uniform extinction in the nebula, which is severe in some places. This is because the optical spectra one uses to derive the average extinction are dominated by the emission from bright and relatively unobscured regions. This may present a potential problem for interpreting observations of very distant unresolved H II regions.

4.3 Large-scale flows, shocks and bubbles

Fig. 5(b) shows an image of the flux ratio of Hα to [O III] λ5007 across the entire Carina Nebula. Ignoring obvious artefacts from bright stars, this gives an excellent view of the large-scale shell structures that define the boundaries of the nebula. Aside from the South Pillar region (see Smith et al. 2000), we draw attention to four main cavities/shells in Carina. The large cavities labelled N and S in Fig. 5(b), seen to the north and south of the main Tr 14 and 16 clusters, are the two halves of what appears to be the main bipolar cavity of the nebula. Additional shells are the northern blister (NB) and the large south-west (SW) shell. There are additional shells as well to the SW direction, as noted by Smith et al. (2000). These shells are reminiscent of the main structural components of 30 Dor (e.g. Wang & Helfand 1991).

OB stars in Carina are distributed around the region, unlike concentrated super star clusters such as NGC 3603 and the Arches cluster in the Galactic Centre (Crowther & Dessart 1998; Figer et al.

1999). However, we can gain some insight into which star clusters blew which bubbles by examining the detailed morphology of the nebula. Much as the proplyds in Orion all point toward θ^1C Ori (e.g. Bally, O'Dell & McCaughrean 2000), Carina contains many dust pillars and cometary clouds, like those discussed by Smith, Bally & Morse (2003a) and Smith et al. (2004b), pointing toward the source of ionization or stellar winds that shaped them. Using unambiguous head–tail structures and well-defined dust pillars as tracers, we measured coordinates and position angles for several 'directional indicators' throughout the Carina Nebula as seen in Hα images from the same data set used by Smith et al. (2003a). For each of these directional indicators, we plot an arrow in Fig. 5(b) over the Hα/[O III] image of the nebula. We find that arrows in the southern S shell, including the South Pillar region, generally point toward η Car and Tr 16 (the lower left of the two stars in Fig. 5b), as do most features along the V-shaped dust lane that bisects the nebula. This includes a few objects that point toward Tr 16, even though they are projected along the line of sight to Tr 14 (see Smith et al. 2003a). Objects within the northern N bubble, on the other hand, point predominantly toward Tr 14. Thus, it is clear that Tr 16 has more influence on the southern parts of the nebula, while the younger Tr 14 cluster currently dominates the excavation to the north.[7]

---

[7] There are, of course, some localized exceptions to these general trends due to projection effects along the line of sight, especially in the brightest inner regions of the nebula. A more detailed examination of such directional indicators and locations of nearby OB stars may illuminate the role of individual stars in shaping their surroundings on various size scales, compared to integrated effects from the larger clusters.

The feature labelled NB in Fig. 5(b) is strange. It is a nearly circular shell-like region, but does not appear to contain any bright OB stars at its centre that drive its expansion. Yet, it has a very high [S II]/Hα ratio (not shown here, except in the colour image in Fig. 1a) that may indicate shock excitation (e.g. Hartigan et al. 1999). We speculate that NB may mark a position where a blister is forming; as the main front advances toward northern Galactic latitudes, it may penetrate through a localized cavity, injecting hot plasma from the H II region's interior through the hole. Consequently, a blister at the edge of the H II region will inflate and the reservoir will eventually pop. The NB feature may be a young version of the larger bubble to the SW (Fig. 5b), which appears to have already broken out to larger distances. The detailed kinematics of these features has not yet been investigated.

4.4 Large-scale triggered star formation and Carina's future prospects

The South Pillars and other adjacent regions of dense nebular material around the periphery of the Carina Nebula (Smith et al. 2000) show clear signs of feedback from massive stars at the centre of the nebula, with numerous dust pillars that point inward (Fig. 5b; see also Smith et al. 2000; Rathborne et al. 2002; Walborn 2002). The morphology in images (Fig. 1) gives the impression that the remnants of a giant molecular cloud are being overrun and shredded by the advancing stellar winds and UV radiation from the stars in Tr 16 and 14 (we do not know what, if anything, triggered the formation of the first generation clusters Tr 14 and 16). Whether or not the formation of the second generation has been triggered by first-generation feedback is not immediately obvious, because one cannot determine from morphology alone whether the advancing front triggered the formation of stars, or if it is simply uncovering dense clumps that would have formed stars anyway. However, we explain here how the scale and character of star formation in Carina may help resolve this ambiguity.

There are several indications that many of the new second-generation stars forming in these South Pillars have ages of $\sim 10^5$ yr or less. The clearest evidence so far comes from young massive outflows and young clusters. The infamous HH 666 jet (Smith et al. 2004a) is a parsec-scale outflow from one of these pillars, showing signs of powerful bursts of episodic mass loss, hinting at a very early evolutionary phase undergoing FU Orionis outbursts (Calvet, Hartmann & Strom 2000). The embedded class I phase implied by the SED of its driving source HH 666IRS is only expected to last $\sim 10^5$ yr. Similarly, most of the stars in the spectacular 'Treasure Chest' cluster (Smith, Stassun & Bally 2005b) found in another pillar appear to lie on isochrones with ages $\sim 10^5$ yr, and the cluster itself has one of the highest disc fractions known among any embedded cluster. There are several other IR sources and young clusters embedded in pillars in Carina (Rathborne et al. 2002, 2004) that have not been studied as thoroughly, but are likely to show similar signs of youth.

This recent star formation in the South Pillars is seen across a region more than half a degree (more than 20 pc) in spatial extent. The sound crossing time for this region is 18 to 20 Myr or more at a speed of $c_s \lesssim 1\,\mathrm{km\,s^{-1}}$ in molecular clouds. In fact, there are (less vigorous) signs of the youngest phases of star formation around the entire periphery of the Carina Nebula cavity across a much larger region of several degrees on the sky (Smith et al. 2000).

The earliest phases of star formation are seen to exist simultaneously across a region where the sound crossing time is more than an order of magnitude longer than the duration of these earliest phases.

Therefore, an external agent is required to synchronize these events. The signal for cloud cores to collapse simultaneously must propagate at a speed much faster than the sound speed in a molecular cloud. Since these sources are all seen near the ionized cavity walls and PDRs of the Carina Nebula, the advancing ionization-shock front is the likely culprit. Alternatively, if star formation were constant and ongoing across the whole Carina molecular cloud complex, we might also expect the youngest population to appear as if it were synchronized (there would be a range of ages present, which would always include some fraction of stars in the youngest observable phases). However, in that scenario, the stars in the youngest phases should be distributed randomly about the cloud – they should not be found preferentially near the heads of dust pillars that are facing inward to the massive stars in the core of the nebula, as observed. Thus, it is the unique combination of suggestive morphology and the large spatial scale across which this occurs in Carina that provides a strong case that these second-generation stars have been directly triggered.

On a global scale, the relative importance of this triggered second generation compared to the first-generation stars in Tr 14 and 16 is not yet clear. The most massive star currently known in this second-generation South Pillar region is CPD-59°2661, which is an O9 V star at the centre of the Treasure Chest cluster (Walsh 1984; Smith et al. 2005b). The pillar containing the Treasure Chest cluster is the brightest of the South Pillars at thermal-IR to mm wavelengths (Smith et al. 2000; Rathborne et al. 2002; K. Brooks et al., in preparation). Yonekura et al. (2005) have identified a few additional molecular cores that may be good candidates for sites of massive star formation. While obscured regions at the periphery of Carina may hide additional late O and early B stars (e.g. Sanchawala et al. 2007), it is unlikely that the South Pillars have recently given birth to large clusters of very massive early O-type stars comparable to Tr 14 and 16. Thus, as star formation cascades to preferentially lower masses, it would appear to be 'petering out' in this second generation that is triggered by stellar winds and radiation from the first one. If true, then the current ongoing star formation is adding mostly low- and intermediate-mass stars to the fledgeling OB association, but not very massive stars. The mass functions in the two regions may be different, but would combine to form the average mass function of the entire OB association. Whether or not this has a significant influence upon the global initial mass function (IMF) from the region depends on the total mass of stars added in the second generation, which has not yet been assessed. Detailed study of this newly recognized second generation in the South Pillars is just beginning, but Carina provides a unique laboratory to investigate this phenomenon.

How long this apparent gentle cascade toward lower mass star formation continues into the future is another matter, however. The massive object η Car gives us a constant reminder that the most massive stars in the region are just now reaching the ends of their lives. Its impending demise will be followed by a dozen or so additional SNe in the next million years, when the WNL, O3 and O4 stars in Carina explode (Paper I). This will suddenly inject 10^{52} to 10^{53} erg of mechanical energy into the region, which is likely to sweep up all remaining nebular mass into dense clouds and trigger further star formation on a massive scale. In Section 3 we estimated that the available reservoir of nebular mass is at least 1–$2 \times 10^6\,\mathrm{M_\odot}$, which is enough to rejuvenate massive star formation in the region. At the present time, the majority of the nebular mass is untapped for star formation because it is in the atomic gas phase in PDRs that are warmed by UV radiation from the central clusters. Less than 30–40 per cent is in molecular clouds that

can form stars. In this way, UV emission currently regulates star formation.

However, after the most luminous stars explode, the UV radiation field will drop precipitously, because it is the few most massive members that dominate the FUV luminosity (Paper I). Their SN shocks will sweep this mass into a dense shell that will no longer be warmed by a strong UV field, and should therefore be more efficient at forming giant molecular clouds and massive stars. Essentially, the disappearance of the UV source plus the shock waves that sweep up the gas *conspire* to enhance the formation of giant molecular clouds. When this conspiracy unfolds, the new generation of massive star formation is likely to produce a ring of OB clusters around the fossil OB association left from Tr 14 and 16 – much like the Gould's Belt and Lindblad ring around the fossil Cas-Tau association in the solar neighbourhood (Blaauw 1991). Thus, the Carina Nebula may provide us with a unique snapshot of an earlier phase in the history of our part of the Galaxy. Specifically, the current phase of second-generation star formation in Carina may be directly relevant for understanding the origin of young stars near the Sun which reside in the interior of Gould's Belt.

There is more to this tale as well. When these multiple SNe from η Car and its siblings occur, the young stars in the second generation at the periphery of the Carina Nebula will have their discs and envelopes pelted by SN ejecta. This will happen soon. The SN ejecta will include short-lived radioactive nuclides such as ^{60}Fe and ^{26}Al, which are found in abundance in meteorites in our Solar system, indicating that the Sun formed in close proximity to a SN (Tachibana & Huss 2003; Hester et al. 2004; Desch & Ouellete 2005). An additional clue that the Sun formed close to massive stars is the clear outer edge of the Kuiper belt (Jewitt, Luu & Trujillo 1998; Allen, Bernstein & Malhotra 2001), since truncated outer edges are a common property of externally evaporated discs in H II regions, such as the famous objects seen in silhouette in the Orion Nebula (McCaughrean & O'Dell 1996; McCaughrean et al. 1998; Bally et al. 2000; Smith et al. 2005a). However, regions like Orion with protoplanetary discs existing close to just a single young O-type star also have significant obstacles to acquiring these short-lived radioactive nuclides. Namely, while these first-generation stars may be very close to the SN, they need to wait 3 Myr or more (about 10 Myr in the case of Orion) before the massive star explodes, during which time their gaseous discs will be mostly evaporated. The stars with protoplanetary discs that are close enough to θ^1C Ori also represent a tiny ($\lesssim$1 per cent) fraction of the surrounding cluster.

These difficulties are alleviated in two important ways in the South Pillars of Carina and similar regions of ongoing star formation at the borders of giant H II regions. First, this second generation of stars that has been triggered by the first is located within a few parsecs of hot massive stars that are already poised to explode, so there will be *no significant delay* between the formation of these second-generation stars and the arrival of ejecta from the SNe. Because the second-generation stars are still young and have large protoplanetary discs, they are able to cast a wider net to trap the short-lived radioactive nuclides, as in the 'aerogel' model of Desch & Ouellete (2005). Second, instead of just one SN like in Orion, Carina will have *dozens of SNe* in just a few million years (there were initially $\sim$70 or more O-type stars in Carina; Paper I). These two properties make a place like the South Pillars a much more likely analogue of the cradle of the Solar system than Sun-like stars forming in first generation clusters (like the protoplanetary discs in the Trapezium of Orion, for example). The probability of this happening depends in part on the ^{60}Fe yield of SNe from very massive stars like η Car, which is poorly constrained (e.g. Smith et al. 2007).

It also depends on the veracity of star formation in regions like the South Pillars, and is of considerable interest for understanding our own origins. For this reason, detailed measurement of the disc fraction, mass function, total mass and other properties of stars forming in the South Pillars is an important goal for future observational studies.

5 SUMMARY AND CONCLUSIONS

We have investigated the energy budget and the global properties of the Carina Nebula on the largest scales of $\sim$3° (across 100–120 pc). Furthermore, we have compared these large-scale properties integrated over the whole nebula with the census of energy input from OB stars in Paper I. (Note that in all estimates here, the radiative energy input and the escaping IR luminosity of the evolved star η Car have been excluded, because η Car's own circumstellar dust shell processes most of its bolometric luminosity.) The main conclusions are summarized here.

1. The integrated IR luminosity of the Carina Nebula measured in *IRAS* and *MSX* data is 1.18×10^7 L$_\odot$. Dust processes about 50–60 per cent of the known radiative luminosity of the OB stars in Carina measured in Paper I.

2. From the integrated 3.4-cm radio continuum flux, we infer a total Lyman continuum photon luminosity of $Q_H = 6.9 \times 10^{50}$ s^{-1}. This is $\sim$75 per cent of the ionizing photon luminosity we derived from a census of Carina's known OB stars in Paper I. Some of the Lyman continuum must therefore escape along with the stellar bolometric luminosity or must get absorbed by dust within the H II region.

3. Using the Hα luminosity as a diagnostic of the ionizing flux, we measured a smaller value of $Q_H = 3 \times 10^{50}$ s^{-1}. This is less than half of that inferred from the radio continuum and 1/3 of the total from stars. The Hα luminosity is significantly absorbed by strong non-uniform extinction that is ignored in a standard average reddening correction.

4. Warm dust at $\sim$80 K, which dominates the integrated SED at 20–30 μm, resides in the interior of the H II region cavity. These are probably large grains mixed with ionized plasma that are heated *in situ* by trapped Lyα from the ionized gas. This warm dust contributes about 1/3 of the total IR luminosity, but contains a negligible fraction of the total dust mass. Based on the similarity of the radio continuum and *MSX* band-E images, we find that diffuse 20–25 μm emission is an excellent tracer of warm dust mixed with ionized gas inside H II regions.

5. Cooler dust at 30–40 K dominates the far-IR emission, the total IR luminosity and the total dust mass of the nebula. From the 35-K component fit to the SED, we measure a total dust mass of $\sim$10^4 M$_\odot$, indicating a likely gas mass associated with this dust of 10^6 M$_\odot$ or more.

6. With this total mass and the ubiquitous $\pm$20 km s^{-1} expansion seen across the nebula, we infer a total kinetic energy in moving gas of at least 8×10^{51} erg. This is only 30 per cent of the available mechanical energy from stellar winds during the 3 Myr lifetime of the nebula. Therefore, on energy grounds, there is no need to invoke a previous SN to explain the kinematics of the region.

7. We find a near-perfect correlation between the 60 μm optical depth and PAH emission seen in the *MSX* band-A image. The only violations of this correlation are point sources with warm circumstellar dust. The PAH emission and 60 μm optical depth have a different spatial distribution than the largest molecular clouds traced by CO emission. The total gas mass traced by $\sim$35-K dust in PDRs

outweighs the total gas mass in molecular clouds. Since these two components have different spatial distributions, we conclude that most of the mass in the nebula resides in atomic gas in PDRs instead of dense molecular clouds, and is therefore not currently participating in star formation. However, the atomic and molecular gas added together provide a substantial reservoir of 1–2×10^6 M$_\odot$ for future star formation.

8. The large sound crossing time of several Myr for the South Pillars is much longer than the $\sim 10^5$-yr duration of the earliest phases of star formation, seen to be synchronized throughout the region. This provides a strong case that much of the ongoing star formation in Carina is indeed triggered, instead of just occurring spontaneously and then being uncovered by the advancing ionization front.

9. The triggered second generation of star formation appears to lack the same scale of high-mass star formation that gave rise to the massive first-generation clusters like Tr 14 and 16. This implies that star formation triggered by stellar winds and UV radiation has a cascading effect, biased toward lower masses. Determining if this is indeed true and how it affects the IMF will be an important aspect of future research in this region. We suspect that the large number of sequential SNe to occur in the near future may conspire with the lack of FUV radiation from those same stars to rejuvenate *massive* star formation, given the large reservoir of atomic and molecular mass still available.

10. Regions like the South Pillars, where a second generation of young stars has been triggered at the periphery of a giant H ɪɪ region, will soon be bombarded with SN ejecta. We argue that these are the best candidates for analogues of the type of environment where the Sun formed, given current constraints from meteoritic evidence of short-lived radioactive nuclides. Dozens of sequential SNe in a short time plus the lack of a delay time between their birth and the arrival of the SN ejecta allow for more efficient injection of short-lived radioactive nuclides in these second-generation triggered regions, as compared to environments like the Trapezium in Orion.

ACKNOWLEDGMENTS

REFERENCES

Allen D. A., Hillier D. J., 1993, Publ. Astron. Soc. Aust., 10, 338
Allen R. L., Bernstein G. M., Malhotra R., 2001, ApJ, 549, L241
Arendt R. G., Dwek E., Moseley S. H., 1999, ApJ, 521, 234
Azcarate I. N., Cersosimo J. C., Colomb F. R., 1981, Rev. Mex. Astron. Astrofis., 6, 269
Bally J., O'Dell C. R., McCaughrean M. J., 2000, AJ, 119, 2919
Blaauw A., 1991, in Lada C. J., Kylafis N. D., eds, The Physics of Star Formation and Early Stellar Evolution. Kluwer, Dordrecht, p. 125
Bouret J. C., Lanz T., Hillier D. J., 2005, A&A, 438, 301
Brooks K. J., Whiteoak J. B., Storey J. W. V., 1998, Publ. Astron. Soc. Aust., 15, 202
Brooks K. J., Burton M. G., Rathborne J. M., Ashley M. C. B., Storey J. W. V., 2000, MNRAS, 319, 95

Brooks K. J., Storey J. W. V., Whiteoak J. B., 2001, MNRAS, 327, 46
Brooks K. J., Cox P., Schneider N., Storey J. W. V., Poglitsch A., Geis N., Bronfman L., 2003, A&A, 412, 751
Brooks K. J., Garay G., Nielbock M., Smith N., Cox P., 2005, ApJ, 634, 436
Buxton M., Bessell M., Watsson R., 1998, Publ. Astron. Soc. Aust., 15, 24
Calvet N., Hartmann L., Strom S. E., 2000, in Mannings V., Boss A. P., Russell S. S., eds, Protostars and Planets IV. Univ. Arizona Press, Tucson AZ, p. 377
Chan K. W., Onaka T., 2000, ApJ, 533, L33
Churchwell E. B. et al., 2006, ApJ, 649, 759
Cox P., 1995, Rev. Mex. Astron. Astrofis. Ser. Conf., 2, 105
Cox P., Bronfman L., 1995, A&A, 299, 583
Cox P., Mezger P. G., Sievers A., Najarro F., Bronfman L., Kreysa E., Haslam G., 1995, A&A, 297, 168
Crowther P. A., Dessart L., 1998, MNRAS, 296, 622
Danks A. C., Walborn N. R., Vieira G., Landsman W. B., Gales J., Garcia B., 2001, ApJ, 547, L155
Deharveng L., Maucherat M., 1975, A&A, 41, 27
Desch S. J., Ouellete N., 2005, Lunar Planet. Sci. Conf., 36, 1327
Egan M. P., Shipman R. F., Price S. D., Carey S. J., Clark F. O., Cohen M., 1998, ApJ, 494, L199
Figer D. F., Kim S. S., Morris M., Serabyn E., Rich R. M., McLean I. S., 1999, ApJ, 525, 750
Fullerton A. W., Massa D. L., Prinja R. K., 2006, ApJ, 637, 1025
Ghosh S. K., Iyengar K. V. K., Rengarajan T. N., Tandon S. N., Verma R. P., Daniel R. P., 1988, ApJ, 330, 928
Grabelsky D. A., Cohen R. S., Bronfman L., Thaddeus P., 1988, ApJ, 331, 181
Hartigan P., Morse J. A., Tumlinson J., Raymond J., Heathcote S., 1999, ApJ, 512, 901
Harvey P. M., Hoffmann W. F., Campbell M. F., 1979, ApJ, 227, 114
Hester J. J., Desch S. J., Healy K. R., Leshin L. A., 2004, Sci, 304, 1116
Hillenbrand L. A., Hartmann L. W., 1998, ApJ, 492, 540
Huchtmeier W. K., Day G. A., 1975, A&A, 41, 153
Jewitt D., Luu J. X., Trujillo C., 1998, AJ, 115, 2125
Kennicutt R. C., 1984, ApJ, 287, 116
Kennicutt R. C., 1998, ARA&A, 36, 189
McCaughrean M. J., O'Dell C. R., 1996, AJ, 111, 1977
McCaughrean M. J. et al., 1998, ApJ, 492, L157
Meaburn J., Lopez J. A., Keir D., 1984, MNRAS, 211, 267
Morris P. et al., 1999, Nat, 402, 502
Muench A. A., Lada E., Lada C. J., Alves J., 2002, ApJ, 573, 366
Price S. D., 1995, Space Sci. Rev., 74, 81
Rathborne J. M., Burton M. G., Brooks K. J., Cohen M., Ashley M. C. B., Storey J. W. V., 2002, MNRAS, 331, 85
Rathborne J. M., Brooks K. J., Burton M. G., Cohen M., Bontemps S., 2004, A&A, 418, 563
Repolust T., Puls J., Herrero A., 2004, A&A, 415, 349
Sanchawala K., Chen W. R., Lee H. T., Chu Y. H., Nakajima Y., Tamura M., Baba D., Sato S., 2007, ApJ, 656, 462
Sanders D. B., Mirabel I. F., 1996, ARA&A, 34, 749
Seward F. D., Chlebowski T., 1982, ApJ, 256, 530
Seward F. D. et al., 1979, ApJ, 234, L55
Simpson J. P., Rubin R. H., 1990, ApJ, 354, 165
Smith N., 2002a, MNRAS, 331, 7
Smith N., 2002b, MNRAS, 337, 1252
Smith N., 2006a, MNRAS, 367, 763 (Paper I)
Smith N., 2006b, ApJ, 644, 1151
Smith N., Gehrz R. D., 2005, AJ, 129, 969
Smith N., Egan M. P., Carey S., Price S. D., Morse J. A., Price P. A., 2000, ApJ, 532, L145
Smith N., Bally J., Morse J. A., 2003a, ApJ, 587, L105
Smith N., Gehrz R. D., Hinz P. M., Hoffmann W. F., Hora J. L., Mamajek E. E., Meyer M. R., 2003b, AJ, 125, 1458
Smith N., Bally J., Brooks K. J., 2004a, AJ, 127, 2793
Smith N., Barbá R. H., Walborn N. R., 2004b, MNRAS, 351, 1457

Smith N., Bally J., Licht D., Walawender J., 2005a, AJ, 129, 382

Smith N., Stassun K. G., Bally J., 2005b, AJ, 129, 888

Smith N. et al., 2007, ApJ, in press (astro-ph/0612617)

Spitzer L. J., 1978, Physical Processes in the Interstellar Medium. Wiley-Interscience, New York

Tachibana S., Huss G. R., 2003, ApJ, 588, L41

Walborn N. R., 2002, in Crowther P., ed., ASP Conf. Ser. Vol. 267, Hot Stars Workshop III: The Earliest Phases of Massive Star Birth. Astron. Soc. Pac., San Francisco, p. 111

Walborn N. R., Hesser J. E., 1975, ApJ, 199, 531

Walborn N. R., Heckathorn J. N., Hesser J. E., 1984, ApJ, 276, 524

Walborn N. R., Smith N., Howarth I. D., Vieira-Kober G., Gull T. R., Morse J. A., 2007, PASP, 119, 156

Walsh J. R., 1984, A&A, 138, 380

Wang Q., Helfand D. J., 1991, ApJ, 370, 541

Whiteoak J. B. Z., 1994, ApJ, 429, 225

Yonekura Y., Asayama S., Kimura K., Ogawa H., Kanai Y., Yamaguchi N., Barnes P. J., Fukui Y., 2005, ApJ, 634, 476

Zhang X., Lee Y., Bolatto A., Stark A. A., 2001, ApJ, 553, 274

This paper has been typeset from a TEX/LATEX file prepared by the author.